Model-based Battery Thermal Fault Diagnostics: Algorithms, Analysis and Experiments

Satadru Dey, *Member, IEEE,* Hector E. Perez, *Member, IEEE,* and Scott J. Moura, *Member, IEEE*

***Abstract*—Safety and reliability remain critical issues for Lithium-ion (Li-ion) batteries. Out of many possible degradation modes, thermal faults constitute a significant part of critical causes that lead to battery degradation and failure. Therefore, it is extremely important to diagnose these thermal faults in real-time to ensure battery safety. Motivated by this fact, we propose a Partial Differential Equation (PDE) model-based real-time scheme in this paper for diagnosing thermal faults in Li-ion batteries. The objective of the diagnostic scheme is to detect and estimate the size of the thermal fault. We utilize a distributed parameter one-dimensional thermal model for cylindrical battery cells in conjunction with PDE observer-based techniques to design the scheme. Furthermore, we apply threshold-based technique to ensure robustness against modeling and measurement uncertainties. The effectiveness of the scheme is illustrated by (i) analytical convergence verification of the PDE observers under heathy and faulty conditions utilizing Lyapunov stability theory, (ii) extensive simulation case studies, (iii) robustness analysis against model parametric uncertainties and, (iv) experimental studies on a commercial Li-ion battery cell.**

***Index Terms*—Lithium-ion Batteries, Thermal Faults, Detection, Estimation, Distributed Parameter Systems.**

I. Introduction

SAFETY and reliability are two critical aspects of Lithium-ion (Li-ion) battery operation. Several failure mechanisms can potentially deteriorate battery safety and reliability. Many of such critical failures manifest themselves as thermal faults in the battery irrespective of their physical origin [1]. A subset of these thermal failures, e.g. thermal runaway, may even lead to catastrophic events if not detected or diagnosed early enough. Therefore, diagnosis of battery thermal failures is extremely important to ensure safe and reliable operation. Motivated by this requirement, we propose a Partial Differential Equation (PDE) model-based diagnosis scheme for thermal faults in Li-ion batteries in this paper.

In the past decade, a substantial body of research has emerged addressing the problem of battery State-of-Charge (SOC) and State-of-Health (SOH) estimation. Several model-based approaches have been proposed for such estimation problems, e.g. Equivalent Circuit Model based approaches [2] [3] [4], Electrochemical Model based approaches [5] [6] [7]. Other than SOC and SOH estimation, battery temperature estimation problems have also started receiving attention since past few years. For example, an adaptive observer is presented for core temperature estimation in [8]. Observer design for temperature estimation in battery packs is studied in [9]. In [10], an internal temperature estimation algorithm is proposed using combined impedance and surface temperature measurements. An estimation algorithm for combined estimation of SOC and internal temperature is presented in [11]. A generic electro-thermal model is proposed in [12] to predict the cell temperature evolution. In [13], an algorithm is presented for estimation of the temperature distribution in cylindrical cells under unknown cooling conditions.

Compared to the control/estimation problems, battery fault diagnosis problems have received significantly less attention in the existing literature. Majority of the existing battery diagnostic approaches rely on limit checking on the measured terminal voltage and surface temperature. However, the main drawbacks of these limit checking approaches are: (i) they may not be able distinguish the effects of abrupt input conditions from faults and, (ii) they may not be able to detect the fault at an early stage when the fault magnitude is smaller and the measurable quantities are within the normal operating limits. On the other hand, model-based diagnostic approaches have the potential to mitigate these limitations significantly by combining models with measurements. Very few efforts have been made in the area of model-based battery diagnostics. Some of the existing model-based approaches deal with sensor and actuator faults [14] [15], electrochemical faults [16], overcharge/over-discharge faults [17]. However, real-time diagnosis of thermal faults is almost unexplored in the existing published literature, despite its critical importance for battery safety and performance. A few efforts exist in battery thermal fault diagnostics. In [14], a one state thermal model capturing the averaged temperature of the battery cell is used to diagnose a cooling system fault. A two-state thermal model capturing the core and surface temperature dynamics is used in [18] to diagnose certain thermal faults. However, the drawbacks of these approaches are: (i) they rely on lumped parameter thermal models which may not be sufficient to capture the effect of distributed thermal faults inside the cell, and (ii) they do not estimate the size of the thermal fault. Note that the information on the thermal fault size can be beneficial for thermal fault-tolerant control of batteries. In our current paper, we extend the aforementioned research works by proposing a PDE model-based thermal diagnostic scheme for Li-ion batteries. The proposed diagnostic scheme is capable of detecting and estimating thermal faults. The proposed PDE-based approach bypasses two possible drawbacks of the

This work was supported in part by the National Science Foundation under Grant No. 1408107.

S. Dey is with the Department of Electrical Engineering, University of Colorado Denver, CO 80204, USA; H. E. Perez and S. J. Moura are with the Energy, Controls, and Applications (eCAL) Laboratory, Department of Civil and Environmental Engineering, University of California, Berkeley, CA 94720, USA. satadru.dey@ucdenver.edu, heperez@berkeley.edu, smoura@berkeley.edu.

Manuscript received xx, 2016.

lumped model-based approaches. First, the lumped models may neglect the higher order but important modes of the system, which in turn may lead to control/observation spillover (for details of the *spillover effect*, please refer to [19]). Second, they unnecessarily intertwine lumping/discretization methods with the analysis and design process. In this particular case, for example, if one realized that a different discretization technique was superior, then they would have to completely re-design and re-analyze the diagnostics observers. Consequently, the generalizability of a lumped model approach is limited in this sense. By synthesizing the observer in the PDE setting, we untangle the design process from the discretization needed for implementation. Hence, no re-design and analysis is necessary in case one finds an alternative discretization method. The current paper extends our preliminary study [20] by: (i) analysis of the robustness of the scheme with respect to model parametric uncertainties; (ii) development of the experimental procedure for thermal fault induction in a Lithium-ion cell, and (iii) demonstration of the effectiveness of the approach using experimental studies.

In the proposed diagnostic scheme, we adopt a one-dimensional distributed parameter thermal model of a cylindrical battery cell [21]. The scheme consists of two PDE observers arranged in cascade and utilizes measured surface temperature feedback. The first observer, denoted as *Robust Observer*, estimates the distributed temperature inside the cell under healthy and faulty conditions. Robust state estimation is a bi-product of this scheme that provides convergent estimates of the temperature distribution inside the battery cell irrespective of healthy or faulty conditions. The second observer, denoted as *Diagnostic Observer*, receives this estimated temperature distribution information from *Robust Observer* and in turn outputs a residual signal that provides the fault information. The backstepping transformation and Lyapunov stability [22] have been utilized to design and analyze the observer. Furthermore, the residual signals are compared with non-zero thresholds to incorporate robustness to modeling and measurement uncertainties. These non-zero thresholds are designed offline based on the probability distribution of the residual signals under a fault-free condition.

The rest of the paper is organized as follows. Section II introduces the distributed parameter thermal model of the battery cell. Section III designs and analyzes the fault diagnosis scheme in detail. Section IV presents simulation and experimental studies. Finally, Section V concludes the work.

Notations: The following notations are used in this paper: $\|u(\cdot)\| = \sqrt{\int_0^1 u^2(x)dx}$, $u_t = \frac{\partial u}{\partial t}, u_x = \frac{\partial u}{\partial x}$, $u_{xx} = \frac{\partial^2 u}{\partial x^2}$.

II. Distributed parameter thermal model for lithium-ion batteries

Nominal Model: We adopt the following (nominal or fault-free) one-dimensional thermal model that predicts the radially distributed temperature dynamics of a cylindrical battery cell [21]:

$$\beta \frac{\partial \bar{T}}{\partial \bar{t}}(r,\bar{t}) = \frac{\partial^2 \bar{T}}{\partial r^2}(r,\bar{t}) + \left(\frac{1}{r}\right)\frac{\partial \bar{T}}{\partial r}(r,\bar{t}) + \frac{\dot{Q}(\bar{t})}{\bar{k}} \quad (1)$$

with Neumann boundary conditions

$$\frac{\partial \bar{T}}{\partial r}(0,\bar{t}) = 0, \quad (2)$$

$$\frac{\partial \bar{T}}{\partial r}(R,\bar{t}) = \frac{h}{\bar{k}}\left(T_\infty - \bar{T}\left(R,\bar{t}\right)\right), \quad (3)$$

where $\bar{t} \in \mathbb{R}^+$ represents time and $r \in [0, R]$ is the spatial coordinate in the radial direction. The parameter $\bar{k}$ is the thermal conductivity of the battery cell, $\dot{Q}(\bar{t})$ is the volumetric heat generation rate, and $\beta = (\rho C_p)/\bar{k}$ is the inverse of thermal diffusivity, where ρ is the mass density and C_p is the specific heat capacity.

Next, we: i) transform the system to the Cartesian coordinate system with spatial coordinate variable $\bar{x}$ and time $\bar{t}$ [23] and, ii) scale the space and time variables in the Cartesian coordinate system by defining $T(x,t) = \bar{T}(\bar{x},\bar{t})$ with $x = \bar{x}/R$, $t = \bar{t}/\beta R^2$ and $k = \bar{k}/R^2$. This transformation and scaling results in the following system, known as a heat equation:

$$T_t(x,t) = T_{xx}(x,t) + \frac{\dot{Q}(t)}{k}, \quad (4)$$

with Neumann boundary conditions

$$T_x(0,t) = 0, \quad (5)$$

$$T_x(1,t) = \frac{h}{k}\left(T_\infty - T\left(1,t\right)\right), \quad (6)$$

where $t \in \mathbb{R}^+$ and $x \in [0, 1]$. The remainder of this paper considers (4)-(6) as the plant model.

Furthermore, we adopt a second order electric circuit model to capture the electrical dynamics of the battery (see Fig. 1) [24]. The electrical circuit consists of an open circuit voltage source (V_{oc}), an internal series resistance (R_{int}) and two resistance-capacitance branches in series. Furthermore, it is assumed that the SOC of the battery is computed online via Coulomb-counting. The state-space equations for the electrical model are:

$$\frac{dSOC}{dt}(t) = -\frac{I(t)}{C_{batt}}, \quad (7)$$

$$\frac{dV_1}{dt}(t) = -\frac{V_1(t)}{R_1 C_1} + \frac{I(t)}{C_1}, \quad (8)$$

$$\frac{dV_2}{dt}(t) = -\frac{V_2(t)}{R_2 C_2} + \frac{I(t)}{C_2}, \quad (9)$$

$$V_{term}(t) = V_{oc}(SOC) - V_1(t) - V_2(t) - R_{int}I(t), \quad (10)$$

where $I(t)$ is the battery current, C_{batt} is the battery charge capacity in Amp-sec and V_{term} is the terminal voltage. The open circuit voltage (V_{oc}) is a function of the State-of-Charge (SOC) and computed online. This function can be determined via offline experimental studies. In this distributed parameter model, R_{int} is assumed to have Arrhenius dependence on the average battery temperature T_{avg} given as:

$$R_{int} = f\left(T_{avg}\right), \quad (11)$$

where $f(T_{avg}) = T_{int,ref}\left[\frac{E_R}{R}\left(\frac{1}{T_{ref}} - \frac{1}{T_{avg}}\right)\right]$ and $R_{int,ref}$ is a known reference value at a known reference temperature T_{ref}. The average temperature of the cell is given by:

$$T_{avg}(t) = \int_0^1 T\left(x,t\right)dx. \quad (12)$$

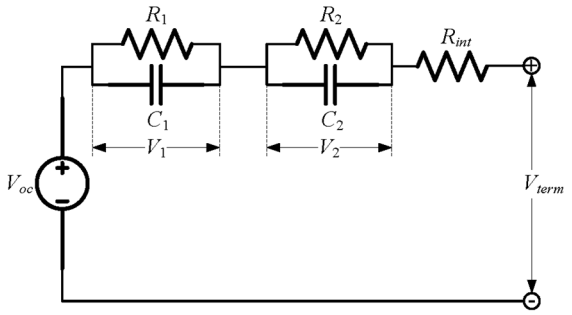

Fig. 1. Battery electrical circuit model

Measurements: Measured variables include the current (I), terminal voltage (V_{term}), and surface temperature $(T(1))$.

Remark 1. The heat generation rate $\dot{Q}$ is expressed as:

$$\dot{Q}(t) = I(t)(V_{oc}(SOC) - V_{term}(t) - T\frac{\partial V_{oc}}{\partial T}). \quad (13)$$

In this work we assume that $\dot{Q}$ is computed online using the measured variables V_{term}, I, and $V_{oc}(SOC)$, which is computed using the SOC information from (7). Furthermore, we assume that the electrical states V_1 and V_2 are computed online via the open-loop model (8)-(9). The term $T\frac{\partial V_{oc}}{\partial T}$ represents the entropic heat generation. The value of the entropic coefficient $\frac{\partial V_{oc}}{\partial T}$ can be found by offline experimental studies [25]. In this work, we consider a Lithium-Iron Phosphate cell for which this entropic coefficient is significantly small [25]. Hence, we ignore the entropic heat generation in the subsequent discussions.

Fault Model: The faulty battery thermal dynamics can be mathematically modeled as

$$T_t(x,t) = T_{xx}(x,t) + \frac{\dot{Q}(t)}{k} + \Delta_Q(x,t), \quad (14)$$

with Neumann boundary conditions

$$T_x(0,t) = 0, \quad (15)$$

$$T_x(1,t) = \frac{h}{k}\left(T_\infty - T\left(1,t\right)\right), \quad (16)$$

where $\Delta_Q(x,t)$ represents a distributed thermal fault.

Remark 2. The fault model $\Delta_Q(x,t)$ in (14) captures the effect of a range of physical failures, e.g. abnormal internal heat generation from electrochemical side reactions, or internal failure due to mechanical or thermal abuse [1][26]. Some of the possible causes of such thermal failures are [26]: i) Internal short circuit caused by separator failure, poor cell design and/or manufacturing; ii) Overcharging may generate abnormal heating due to oxidative chemical reactions; iii) External physical damage such as shock, puncture or vibration can create short circuit in the battery cell leading to thermal runaway condition; iv) Battery cells with flammable electrolyte may cause secondary fire when the cell packaging is damaged due to external physical abuse. Most of these failures are essentially manifested by an abnormal heat generation in the cell which is represented by the term $\Delta_Q(x,t)$.

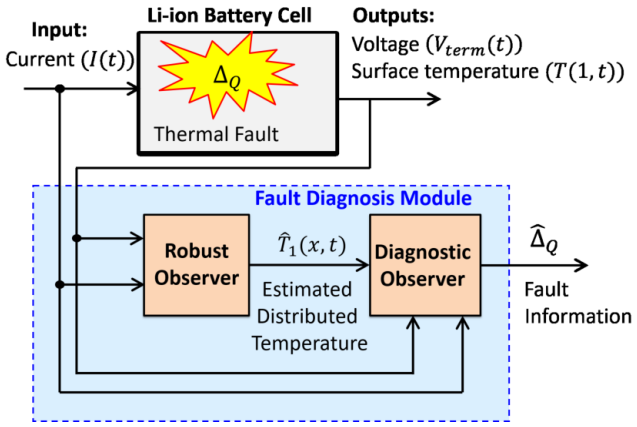

Fig. 2. Fault diagnosis scheme.

Assumption 1. We assume that only one fault can occur at a time, i.e. no multiple faults. Furthermore, we focus on fault detection and estimation. Isolation of multiple faults is not an objective of the present work and subjected to future research.

III. Fault Diagnosis Scheme

The fault diagnosis scheme is diagramed in Fig. 2. The scheme consists of two observers working in a cascaded manner. The first observer, *Robust Observer*, uses the surface temperature feedback and estimates the distributed battery cell temperature under healthy (non-faulty) and faulty conditions. The second observer, *Diagnostic Observer*, receives the estimated temperature distribution from *Robust Observer* and in turn provides a residual signal. The residual signal is used for detection and estimation of the thermal fault (Δ_Q). In the next subsections, we will discuss the design and analysis of these two observers in detail.

Remark 3. The proposed diagnostic scheme provides an accurate estimation of the temperature distribution inside the battery cell irrespective of faulty or healthy condition. This is an added beneficial feature of the scheme.

A. Robust observer

The following structure is chosen for the *Robust Observer*,

$$\hat{T}_{1t}(x,t) = \hat{T}_{1xx}(x,t) + \frac{\dot{Q}(t)}{k} + P_1(x)\tilde{T}_1(1,t), \quad (17)$$

with Neumann boundary conditions

$$\hat{T}_{1x}(0,t) = 0, \quad (18)$$

$$\hat{T}_{1x}(1,t) = \frac{h}{k}\left(T_\infty - T\left(1,t\right)\right) + P_{10}\tilde{T}_1(1,t), \quad (19)$$

where $\hat{T}_1(x,t)$ is the estimated temperature distribution, $\tilde{T}_1(1,t) = T(1,t) - \hat{T}_1(1,t)$ is the boundary estimation error and $P_1(x)$ and P_{10} are the observer gains to be determined.

The error dynamics of the *Robust Observer* are given by subtracting (17)-(19) from (14)-(16),

$$\tilde{T}_{1t}(x,t) = \tilde{T}_{1xx}(x,t) + \Delta_Q(x,t) - P_1(x)\tilde{T}_1(1,t), \quad (20)$$

$$\tilde{T}_{1x}(0,t) = 0, \tag{21}$$
$$\tilde{T}_{1x}(1,t) = -P_{10}\tilde{T}_1(1,t). \tag{22}$$

Next, we follow the backstepping approach to analyze the error dynamics and design the observer gains $P_1(x), P_{10}$ [22]. The backstepping approach seeks the linear Volterra transformation $\tilde{T}_1(x,t) \mapsto \omega(x,t)$

$$\tilde{T}_1(x,t) = \omega(x,t) - \int_x^1 P(x,y)\omega(y,t)dy, \tag{23}$$

which transforms (20)-(22) to the following target error system

$$\omega_t(x,t) = \omega_{xx}(x,t) + \Delta_{\omega Q}(x,t) - c\omega(x,t), \tag{24}$$
$$\omega_x(0,t) = 0, \tag{25}$$
$$\omega_x(1,t) = 0, \tag{26}$$

with $c > 0$ as a parameter of user's choice and $\Delta_Q(x,t) = \Delta_{\omega Q}(x,t) - \int_x^1 P(x,y)\Delta_{\omega Q}(y,t)dy$. One can show the gain kernel $P(x,y)$ in (23) must satisfy the following PDE [22]:

$$P_{yy}(x,y) - P_{xx}(x,y) = cP(x,y), \tag{27}$$

for $(x,y) \in \mathbb{D} = \{x,y : 0 < y < x < 1\}$ with boundary conditions

$$P(x,x) = -c\frac{x}{2}, \tag{28}$$
$$P_x(0,y) = 0, \tag{29}$$

and the observer gains can be computed as:

$$P_1(x) = -P_y(x,1), \tag{30}$$
$$P_{10} = -P(1,1), \tag{31}$$

The expressions for the kernel PDE (27)-(29) and observer gain conditions (30)-(31) can be derived following the steps given in Section 5.3 of [22].

Remark 4. There exists a unique and closed-form solution of the kernel PDE (27)-(29) [22], given by

$$P(x,y) = -cy\frac{I_1(\sqrt{c(y^2-x^2)})}{\sqrt{c(y^2-x^2)}}. \tag{32}$$

where $I_1(.)$ is first order modified Bessel function. Therefore, the observer gains can be computed offline via (30)-(31) using the closed form solution (32).

Remark 5. It can be proven that the transformation (23) is invertible [22]. Hence, stability of the target system (24)-(26) implies stability of the original system (20)-(22). Next, we present a theorem for the convergence of the *Robust Observer* via stability analysis of the target system.

Theorem 1 (Convergence of Robust Observer)**.** *Consider the error dynamics (24)-(26). If $c > 0$, then*
(a) under Scenario 1: $\Delta_{\omega Q} = 0$ i.e. in the presence of no fault, the origin of the error dynamics $\omega(x,t) = 0$ is exponentially stable in the sense of the spatial $\mathcal{L}_2$ norm, and
(b) under Scenario 2: $\Delta_{\omega Q} \neq 0$ i.e. in the presence of a fault, the error $\omega(x,t)$ remains bounded in the sense of spatial $\mathcal{L}_2$ norm defined by $R_B \triangleq \frac{\|\Delta_{\omega Q}\|}{c}$ as $t \to \infty$,
where c is the user-defined parameter, $\Delta_{\omega Q}$ is the fault and $\omega(x,t)$ is the distributed estimation error defined in (24).

Remark 6. Note that the magnitude of R_B can be made arbitrarily small by choosing c arbitrarily large. However, in practical implementation, arbitrarily higher values of c will amplify measurement noise and might lead to instability of the observer dynamics. This trade-off should be considered while tuning the parameter c.

Proof. We consider the square of the spatial $\mathcal{L}_2$ norm of the error as a Lyapunov function candidate to analyze the error dynamics (24)-(26):

$$W_1(t) = \frac{\|\omega\|^2}{2} \triangleq \frac{1}{2}\int_0^1 \omega^2(x,t)dx. \tag{33}$$

The derivative of $W_1(t)$ along the state trajectory can be written as:

$$\dot{W}_1(t) = \int_0^1 \omega\omega_t dx. \tag{34}$$

Now consider the right hand side of (34),

$$\int_0^1 \omega\omega_t dx = \int_0^1 \omega\omega_{xx}dx + \int_0^1 \omega\Delta_{\omega Q}dx - c\int_0^1 \omega^2 dx. \tag{35}$$

Applying integration by parts on the first term and the Cauchy-Schwarz inequality on the second term of the right hand side of (35) yields

$$\int_0^1 \omega\omega_t dx \leq -\|\omega_x\|^2 + \|\omega\|\,\|\Delta_{\omega Q}\| - c\|\omega\|^2 \tag{36}$$

Now, considering (36) we can write the upper bound of the derivative of the Lyapunov function

$$\dot{W}_1(t) \leq \|\omega\|\,(\|\Delta_{\omega Q}\| - c\|\omega\|). \tag{37}$$

Now considering *Scenario 1:* $\Delta_{\omega Q} = 0$, we can write (37) as

$$\dot{W}_1(t) \leq -2cW_1(t). \tag{38}$$

If $c > 0$ the comparison principle applied to (38) gives $W_1(t) \leq W_1(0)\exp(-2ct)$, which confirms the exponential convergence of $W_1(t)$. Hence, the origin of the error dynamics $\omega(x,t) = 0$ is exponentially stable in the sense of the spatial $\mathcal{L}_2$ norm.
Next, we consider *Scenario 2:* $\Delta_{\omega Q} \neq 0$. From (37), the sufficient conditions for the negative definiteness of $\dot{W}_1(t)$ are

$$\|\omega\| > \frac{\|\Delta_{\omega Q}\|}{c}. \tag{39}$$

Squaring both sides of the condition in (39), we can write the sufficiency condition as:

$$\|\omega\|^2 > R_B^2 \triangleq \frac{\|\Delta_{\omega Q}\|^2}{c^2}. \tag{40}$$

Therefore, we can conclude that the negative definiteness of $\dot{W}_1(t)$ will hold outside the ball of radius in the $\|\omega\|_{\mathcal{L}_2}$ space defined by R_B. Hence, $W_1(t)$ will settle on or within a bounded ball of radius $\frac{R_B^2}{2}$. This implies $\|\omega\|_{\mathcal{L}_2} \leq R_B$ as $t \to \infty$. Note that the magnitude of R_B can be made arbitrarily small by choosing a high value of c. □

Remark 7. In the above analysis, the robustness of the *Robust Observer* is with respect to the fault as it suppresses the fault effect to provide reasonably accurate estimate of distributed

temperature. However, the robustness with respect to additive uncertainty in the PDE dynamics can be easily shown. Essentially, the same analysis applies with one modification: the term $\Delta_Q(x,t)$ in (20) would capture both the additive fault and additive uncertainties.

Remark 8. The upper bound of the error in terms of original error variable $\tilde{T}(x,t)$ can be derived in the following way. The second term on the right hand side of (23) can be bounded by:

$$-\int_x^1 P(x,y)\omega(y,t)dy \leq \int_0^1 |P(x,y)|\,|\omega(y,t)|\,dy \leq P_{max}\int_0^1 |\omega(y,t)|\,dy = P_{max}\int_0^1 |\omega(x,t)|\,dx, \quad (41)$$

where $P_{max} = max_{x,y\in[0,1]}|P(x,y)|$. From Cauchy-Schwartz inequality, we have $\int_0^1 |\omega(x,t)|\,dx \leq \|\omega\|$. Therefore, from (41) and Theorem 1 we can write

$$-\int_x^1 P(x,y)\omega(y,t)dy \leq P_{max}\|\omega\| \leq P_{max}R_B. \quad (42)$$

Applying the bound (42) on (23), we have

$$\tilde{T}_1(x,t) \leq \omega(x,t) + P_{max}R_B. \quad (43)$$

Applying triangle inequality on (43), we can find the following upper bound $\left\|\tilde{T}\right\| \leq R_B(1+P_{max})$.

B. Diagnostic observer

The *Diagnostic Observer* utilizes the estimated temperature distribution from *Robust Observer* as a feedback signal.

Assumption 2. The estimated temperature distribution from *Robust Observer* can be written as:

$$\hat{T}_1(x,t) = T(x,t) + \epsilon(x,t).$$

where $\epsilon(x,t)$ represents the estimation error. However, we have proven that ϵ can be made arbitrarily small by selecting c arbitrarily large. Therefore, we assume $\hat{T}_1(x,t) \approx T(x,t)$ for all practical purposes in the following analysis.

Assumption 3. We assume the following structure of the fault function

$$\Delta_Q(x,t) = \theta \cdot \psi(x, T(x,t), I(t)) \quad (44)$$

where $\psi(\cdot,\cdot,\cdot)$ is a known basis function of space x, distributed state $T(x,t)$ and input current I, and $\theta \in \mathbb{R}$ is an unknown constant parameter which determines the fault size or intensity. The main objective of the diagnostic observer is to estimate the value of θ.

Remark 9. The assumption of known basis function $\psi(\cdot,\cdot,\cdot)$ enables the application of adaptive observer framework. Essentially, the idea behind Assumption 3 is to separate the fault information into two parts: a known part (basis function) and an unknown part (fault intensity). Estimation of distributed fault may not be possible if the fault characteristics are completely unknown. Hence, we assume at least the basis function is known. With the knowledge of this known basis function, we estimate the unknown fault intensity. In practice, the basis function of the fault should be identified offline based on the thermal Failure Mode and Effect Analysis (FMEA). For example, the knowledge about thermal hot-spots regarding micro short circuit faults can be utilized to formulate the basis function [27].

Considering *Assumption 2* and *Assumption 3*, the following structure is chosen for the *Diagnostic Observer*,

$$\hat{T}_{2t}(x,t) = \hat{T}_{2xx}(x,t) + \frac{\dot{Q}(t)}{k} + \hat{\theta}\psi(x,T(x,t),I(t)) + L_2\tilde{T}_2(x,t), \quad (45)$$

with Neumann boundary conditions

$$\hat{T}_{2x}(0,t) = 0, \quad (46)$$

$$\hat{T}_{2x}(1,t) = \frac{h}{k}\left(T_\infty - T\left(1,t\right)\right), \quad (47)$$

where $\hat{T}_2(x,t)$ is the estimated temperature distribution by *Diagnostic Observer*, $\tilde{T}_2(x,t) = T(x,t) - \hat{T}_2(x,t)$ is the distributed estimation error with $T(x,t)$ as the estimated temperature distribution from *Robust Observer*, $\hat{\theta}$ is the estimated size of the fault and, $L_2 \in \mathbb{R}$ is an observer gain to be determined. The update law for $\hat{\theta}$ is chosen as

$$\dot{\hat{\theta}} = \frac{1}{L_3}\int_0^1 \psi(x,T(x,t),I(t))\tilde{T}_2(x,t)dx, \quad (48)$$

where $L_3 > 0$ is a user-defined gain that determines the parameter convergence rate. Subtracting (45)-(47) from (14)-(16), we can write the error dynamics of *Diagnostic Observer* as

$$\tilde{T}_{2t}(x,t) = \tilde{T}_{2xx}(x,t) + \tilde{\theta}\psi(x,T(x,t),I(t)) - L_2\tilde{T}_2(x,t), \quad (49)$$

with Neumann boundary conditions

$$\tilde{T}_{2x}(0,t) = \tilde{T}_{2x}(1,t) = 0, \quad (50)$$

where $\tilde{\theta} = \theta - \hat{\theta}$. In the following theorem, we analyze the performance of the *Diagnostic Observer*.

Theorem 2 (Performance of Diagnostic Observer)**.** *Consider the error dynamics (49)-(50) and the parameter update law (48). If Assumption 2 and Assumption 3 are valid and $L_2 \geq -\frac{1}{4}$, $L_3 > 0$, then the distributed state estimation error $\tilde{T}_2(x,t)$ and parameter estimation error $\tilde{\theta}$ will be bounded. i.e. $\left\|\tilde{T}_2\right\|, \left|\tilde{\theta}\right| \in \mathbb{L}_\infty$ as $t \to \infty$,*
where L_2 is the observer gain defined in (45) and parameter update law gain, L_3 is the gain in parameter update law (48), $\tilde{T}_2(x,t)$ and $\tilde{\theta}$ are the state and parameter estimation error defined in (49).

Proof. We consider the following Lyapunov function candidate to analyze the error dynamics

$$W_2(t) = \frac{1}{2}\int_0^1 \tilde{T}_2^2(x,t)dx + \frac{L_3}{2}\tilde{\theta}^2 \quad (51)$$

The derivative of $W_2(t)$ along the state trajectories can be written as:

$$\dot{W}_2(t) = \int_0^1 \tilde{T}_2\tilde{T}_{2t}dx + L_3\tilde{\theta}\dot{\tilde{\theta}} \quad (52)$$

Now considering (49) and the fact $\dot{\theta} = 0$, we can write

$$\begin{aligned}\dot{W}_2(t) = &\int_0^1 \tilde{T}_2\tilde{T}_{2xx}dx - L_2\int_0^1 \tilde{T}_2^2 dx \\ &+\tilde{\theta}\int_0^1 \psi(x,T,I)\tilde{T}_2 dx - L_3\tilde{\theta}\dot{\tilde{\theta}}\end{aligned} \tag{53}$$

Next applying integration by parts on the first term of the right hand side of (53) and then applying Poincaré inequality: $-\int_0^1 \tilde{T}_{2x}^2 dx \leq -\frac{1}{4}\int_0^1 \tilde{T}_2^2 dx$, we have

$$\begin{aligned}\dot{W}_2(t) \leq &-\frac{1}{4}\int_0^1 \tilde{T}_2^2 dx - L_2\int_0^1 \tilde{T}_2^2 dx \\ &+\tilde{\theta}\int_0^1 \psi(x,T,I)\tilde{T}_2 dx - L_3\tilde{\theta}\dot{\tilde{\theta}}\end{aligned} \tag{54}$$

Finally, applying the update law (48) on (54), we can write:

$$\dot{W}_2(t) \leq -\left(\frac{1}{4} + L_2\right)\int_0^1 \tilde{T}_2^2 dx. \tag{55}$$

From (55) it can be concluded that $\dot{W}_2(t)$ is negative semidefinite if $L_2 \geq -\frac{1}{4}$. Hence, the estimation errors $\left|\tilde{\theta}\right|$ and $\tilde{T}_2(x,t)$ will be bounded. i.e. $\left\|\tilde{T}_2\right\|, \left|\tilde{\theta}\right| \in \mathbb{L}_\infty$ as $t \to \infty$.

□

Remark 10. The parameter estimate $\hat{\theta}$ will be used as a residual signal which serves the purpose of detection (indicated by $\hat{\theta} \neq 0$) and estimation (indicated by the magnitude of $\hat{\theta}$) of the thermal fault Δ_Q.

Remark 11. For improved accuracy of fault models, it is possible to modify the fault structure (44) as:

$$\Delta_Q(x,t) = \sum_{i=1}^{N} \theta_i \cdot \psi_i(x) \tag{56}$$

where $\psi_i(x)$ can be chosen as typical basis functions like trigonometric functions, exponential or Gaussian function. The modified fault structure contains more free parameters $(\theta_i, \psi_i(\cdot))$ and hence will be able to capture more complex fault distributions as compared to the fault structure in (44). However, the design and analysis of the *Diagnostic Observer* will remain same even with the modified fault structure. Referring to Theorem 2, with the choice of Lyapunov function candidate $W_2(t) = \frac{1}{2}\int_0^1 \tilde{T}_2^2(x,t)dx + \sum_{i=1}^{N}(L_{3i}/2)\tilde{\theta}_i^2$, the update law becomes $\dot{\hat{\Theta}} = L\Psi$ where $\Theta = [\theta_1, ..., \theta_N]^T$, $L = diag(\frac{1}{L_{31}}, ..., \frac{1}{L_{3N}})$, $\Psi = [\int_0^1 \psi_1(x)\tilde{T}_2(x,t)dx, ..., \int_0^1 \psi_N(x)\tilde{T}_2(x,t)dx]^T$ with $diag(.)$ denoting a diagonal matrix.

Remark 12. The presence of uncertainties (unmodeled dynamics and measurement noise) prohibits the residual $\hat{\theta}$ from having the idealized property of equaling zero in the absence of a fault. We handle the effect of uncertainties by comparing the residual with nonzero thresholds. The residuals are be evaluated as follows: A fault is detected when $\hat{\theta} > th$; no fault when $\hat{\theta} \leq th$, where th is the predefined threshold. The effect of the uncertainties on the residuals will be suppressed below these threshold values. The threshold can be designed using the following equation:

$$P_{FA} = \int_{-\infty}^{-th} p_0(x)\,dx + \int_{th}^{\infty} p_0(x)\,dx \tag{57}$$

where P_{FA} is the probability of false alarm (defined by the user), th is the selected threshold and $p_0(x)$ is the residuals probability distribution under no fault. The distribution $p_0(x)$ can be found by collecting residual data under non-faulty conditions from Monte-Carlo simulations or experimental studies.The goal here is to select th which will yield an user-defined acceptable P_{FA}. It is important to note that a smaller choice of threshold may lead to improved detectability of the fault, however, at the cost of higher false alarm rates. The threshold design process remains same for the fault structure in Assumption 3 and Remark 11 with the following exception: N thresholds would be needed for the fault structure in Remark 11 (one threshold for each θ_i).

IV. Simulation and Experimental studies

In this section, we conduct simulation and experimental studies to evaluate the performance of the proposed scheme. We start with identifying the battery model parameters utilizing the experimental data collected from a commercial Li-ion battery cell. The battery under consideration is a commercial Lithium Iron Phosphate A123 26650 cylindrical cell with rated capacity of 2.3 Ah. Note that, the electrical and thermal model parameters have each been identified in [24] and [13], respectively. However, due to variability in manufacturing, cooling and other operating conditions, some of the crucial thermal and electrical parameters can vary from cell to cell. Therefore, we re-identify some of the parameters by solving parameter fitting optimization formulation using Particle Swarm Optimization (PSO) and data generated from our experimental facility. Essentially, PSO minimizes the Root Mean Square (RMS) error between the model and experimental voltage and temperature data by optimizing the values of the following thermal and electrical parameters: h, $R_{int,ref}$, R_1, R_2, C_1, C_2 and C_{batt}. The resulting values of the thermal and electrical parameters are given in Table I.

The experimental setup includes a cell placed on an Arbin High Current Cylindrical Cell Holder inside of an ESPEC BTL-433 environmental chamber to regulate the ambient temperature at 25°C (298.15K). An OMEGA K-Type Thermocouple (SA1-K-120) is placed on one side of the surface of the battery to measure the surface temperature of the cell $T(1,t)$, and an OMEGA Silicone Rubber Heating Pad (SRFG-101/10) is placed on the other side of the surface to emulate heat generation faults Δ_Q as shown in Fig. 3. A PEC SBT2050 cycler is used to control the input current to the battery. In Fig. 4 and Fig. 5, a comparison between the open-loop identified model and the experimental data is shown for voltage and surface temperature under no fault condition. The Root Mean Square (RMS) error values for this case are 27 mV and 0.2° C. Next, we utilize this identified model for simulation and experimental fault diagnosis studies.

TABLE I
THERMAL AND ELECTRICAL PARAMETERS. (I) DENOTES IDENTIFIED VALUES FOR THIS SPECIFIC STUDY.

Parameters	Values	Parameters	Values
ρ	2047 kg/m^3 [13]	C_{batt}	2.26 Ah (I)
C_p	1109.2 J/kgK [13]	C_1	3260.9 F (I)
k	0.610 W/mK [13]	C_2	5314.9 F (I)
h	69.89 W/m^2K (I)	R_1	0.0029 Ω (I)
$R_{int,ref}$	0.015 Ω (I)	R_2	0.0021 Ω (I)

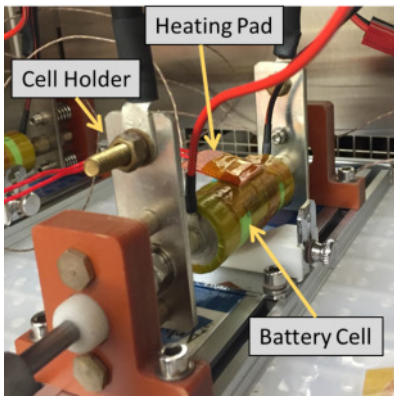

Fig. 3. Fault emulating experimental setup.

A. Simulation studies

This section discusses several simulation studies. Simulation studies enable us to rapidly study a wide variety of fault conditions that might be costly, difficult, timely, or impractical to perform experimentally. In simulation, the applied current and corresponding voltage response are shown in Fig. 4, under no fault condition. The temperature distribution is shown in Fig. 6. To emulate measurement uncertainty, we inject zero mean Gaussian noises in the measured quantities: $10mA$ current (I) noise, 0.3°C surface temperature (T_s) noise and $5mV$ voltage (V_{term}) noise. Under these assumed uncertainties, we select a constant threshold value for the residual signal $(\hat{\theta})$ following the procedure discussed in the previous section. In the following results, the performance of the observers will be shown in terms of spatially averaged temperature, i.e. $T_{avg} = \int_0^1 T(x,t)dx$ and $\hat{T}_{i-avg} = \int_0^1 \hat{T}_i(x,t)dx$ where $T(x,t)$ represents actual temperature and $\hat{T}_i(x,t)$ represent estimated temperatures with $i \in \{1,2\}$. Furthermore, we will quantify the convergence performance of the estimates in terms of (i) *steady-state error* and, (ii) *convergence time*, defined as the time taken to reach within $\pm 2\%$ band of the true value starting from the incorrect initial condition. The observer estimates are provided in Fig. 7 under no fault condition. To verify the convergence properties, both the observers are initialized with incorrect temperature 295 K, 3 K less than the true initial condition of 298 K. Recall from Theorem 1 that we have proven exponential stability of $\tilde{T}_1(x,t)$ to the origin, in the sense of the spatial $\mathcal{L}_2$ norm. Theorem 2 proves boundedness of the $\mathcal{L}_2$ norm of $\tilde{T}_2(x,t)$, i.e. $\|\tilde{T}_2\| \in \mathbb{L}_\infty$. In Fig. 7, both $\hat{T}_{1-avg}$ and $\hat{T}_{2-avg}$ from the *Robust Observer* and *Diagnostic Observer*, respectively, converge to the true

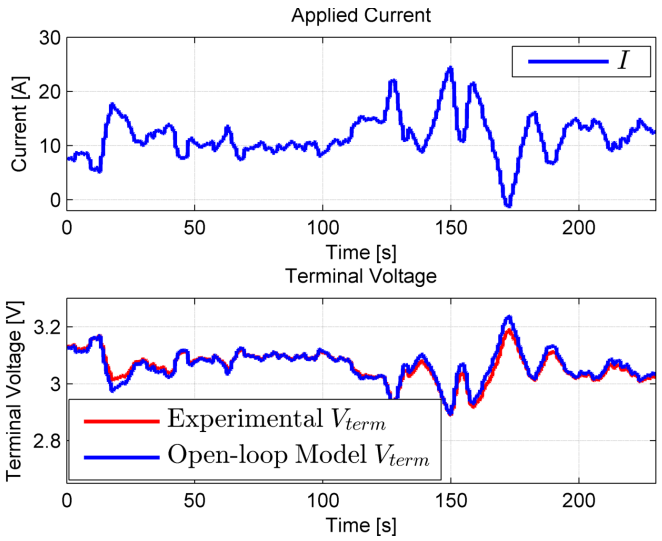

Fig. 4. Applied current and comparison of experimental and open-loop model terminal voltage under no fault condition. Positive current corresponds with discharge. Root mean square voltage error is 27 mV.

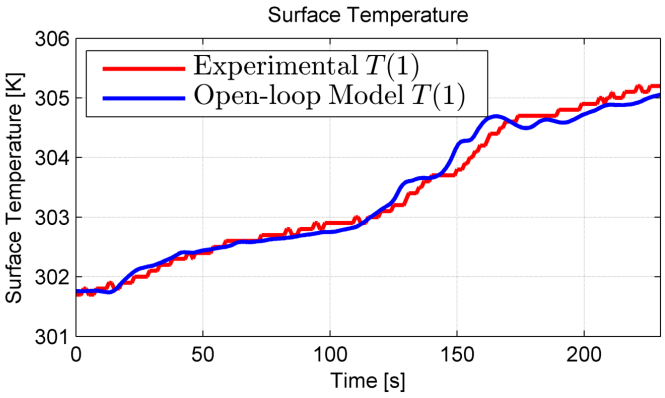

Fig. 5. Comparison of experimental and open-loop model surface temperature under no fault condition. Root mean square temperature error is 0.2 °C.

temperature T_{avg}. The convergence time for both observers are within 0.1 sec with zero steady-state error.

Next we illustrate the effectiveness of the proposed approach under the following faulty cases.

Case 1: A constant and uniformly distributed additive heat generation fault is injected between 50 sec and 170 sec in the battery. In this case we have $\psi(x,T(x,t),I(t)) = 1$ and $\Delta_Q(x,t) = \theta$. The nature of the fault is abrupt/step-like. The threshold is chosen $th = 0.02$. The temperature distribution is shown in Fig. 8, which clearly exhibits higher temperatures than Fig. 6. The corresponding performance of the observers (in terms of estimated average temperature and estimation error) is provided in Fig. 9. Similar to the nominal case, both observers are initialized with incorrect temperatures to test the convergence properties. In Fig. 9, both $\hat{T}_{1-avg}$ and $\hat{T}_{2-avg}$ from the *Robust Observer* and *Diagnostic Observer*, respectively, converge to the true temperature T_{avg}. The convergence time for both observers are within 0.1 sec with less than 0.2^oC steady-state error. This is expected, of course, since the fault does not occur until 50sec. Furthermore, the

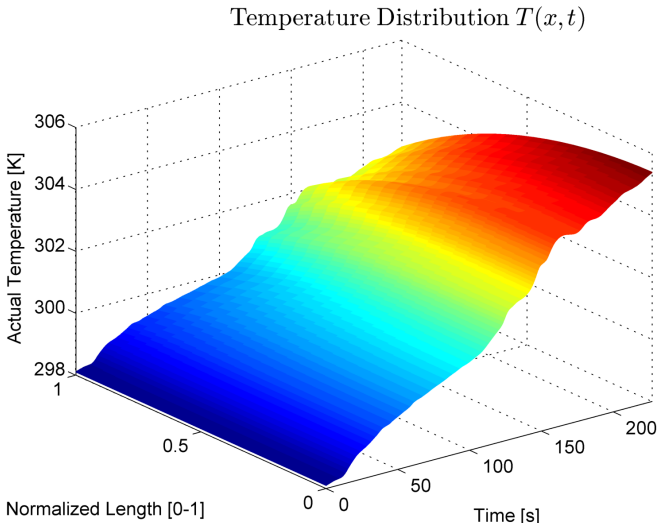

Fig. 6. Radial temperature distribution under no fault condition.

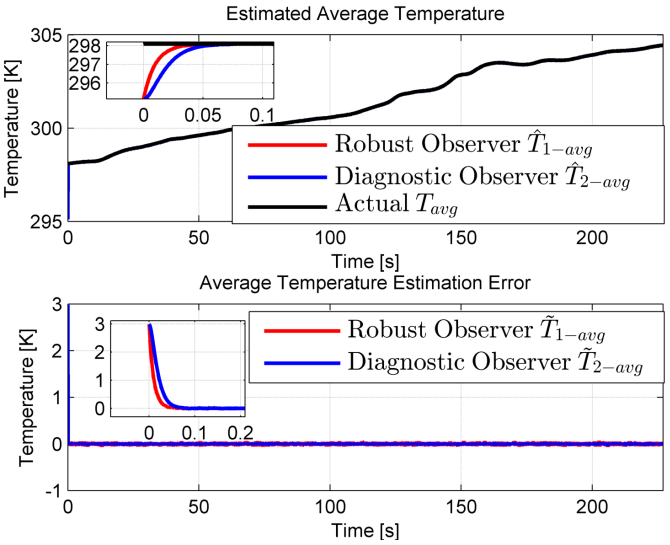

Fig. 7. Temperature estimation performance under no fault condition. The convergence time to reach within $\pm 2\%$ band of the true temperature is less than 0.1 sec for both observers.

fault estimation parameter $\hat{\theta}$ crosses the threshold shortly after the fault occurrence at 50 sec, thus detecting the fault. Moreover, $\hat{\theta}$ converges to a neighborhood of the true fault size θ, as shown in the bottom subplot in Fig. 9. Recall that Theorem 2 only guarantees boundedness of $\tilde{\theta}$, i.e. $|\tilde{\theta}| \in \mathbb{L}_\infty$. Nevertheless, we find the estimate can be successfully used to estimate fault size. In this case, the detection time is 1 sec whereas the fault estimate ($\hat{\theta}$) converges to the true value (θ) within 5 sec. In addition, convergence of both observer estimates $\hat{T}_{1-avg}$, $\hat{T}_{2-avg}$ remains robust to the fault presence.

Case 2: In this case, we study an local internal short circuit fault. Unlike previous case where the fault is uniformly distributed over the spatial domain, the local fault occurs only at a sub-region of the spatial domain. The fault has been injected at 300 sec under $5A$ constant current. In this case, we have $\Delta_Q(x,t) = \theta\psi(x, T(x,t), I(t))$ where $\theta = I_{sc}^2 R_{sc}$

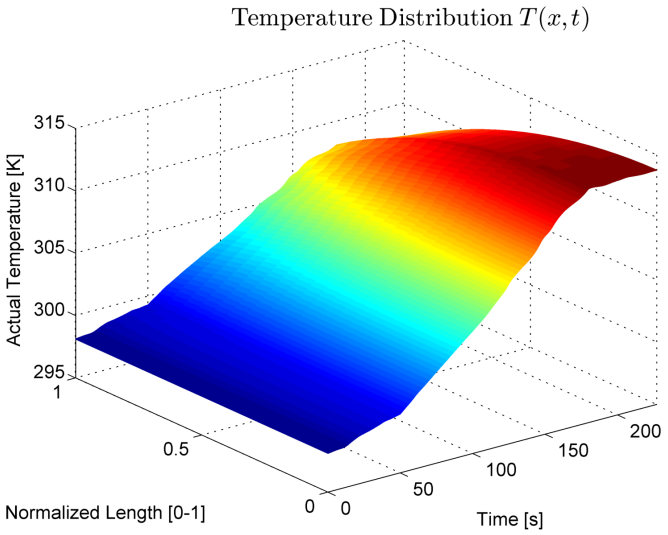

Fig. 8. Temperature distribution inside the battery under faulty condition. The fault is injected between 50 sec and 170 sec. Nature of the fault: abrupt.

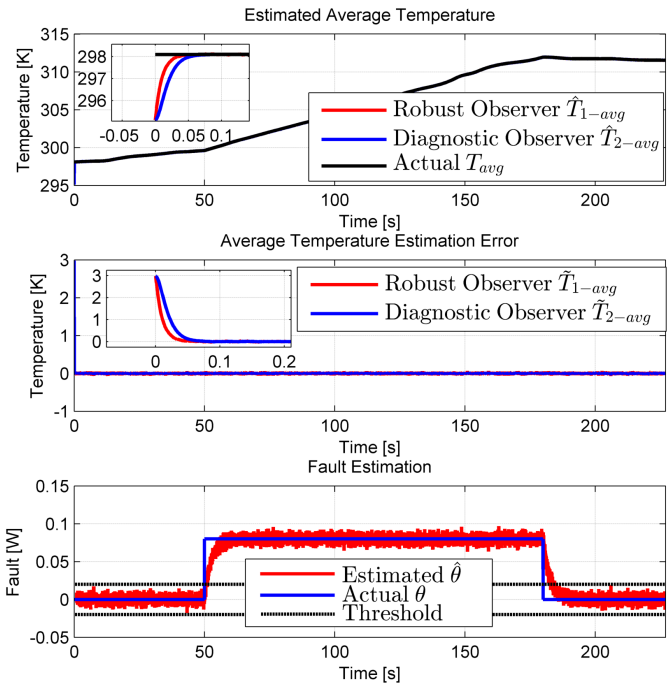

Fig. 9. Temperature and fault estimation performance under fault case 1. The fault is injected between 50 sec and 170 sec. Nature of the fault: abrupt.

with $I_{sc} = 25A$ as the short circuit current and $R_{sc} = 40m\Omega$ is the short circuit resistance, and $\psi(\cdot,\cdot,\cdot)$ is a trapezoidal function that captures the local fault distribution. In this case, $\psi(\cdot,\cdot,\cdot)$ is only a function of space and hence denoted by $\psi(x)$. The same threshold is used $th = 0.02$. Temperature response under the fault is shown in Fig. 10. Fault estimation performance along with the basis function $\psi(x)$ is shown in Fig. 11. It can be noted that the fault estimation parameter $\hat{\theta}$ crosses the threshold shortly after the fault occurrence at 300 sec, signaling a detected fault. Furthermore, $\hat{\theta}$ accurately estimates the fault magnitude θ. The detection time is 0.4 sec and the fault estimate ($\hat{\theta}$) converges to the true value (θ)

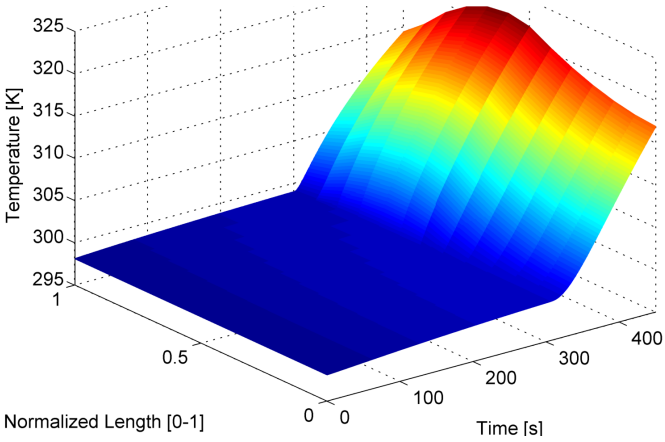

Fig. 10. Temperature distribution inside the battery under the local internal short circuit fault. The fault is injected at 300 sec. Nature of the fault: abrupt.

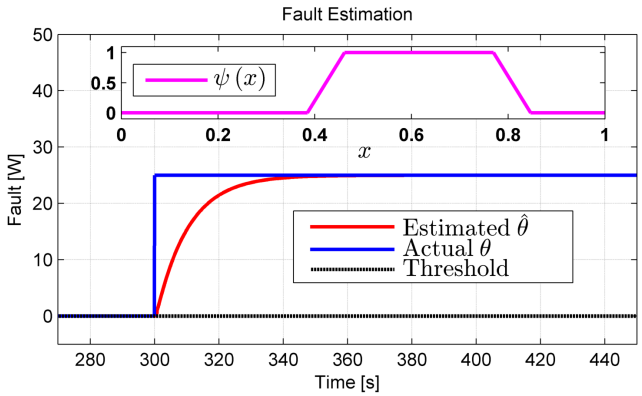

Fig. 11. Fault estimation performance under the local internal short circuit fault. The fault is injected at 300 sec. Nature of the fault: abrupt.

within 40 sec. Note that the scheme can detect and estimate the fault if the short circuit current I_{sc} is slowly varying (as we have assumed θ is fairly constant or slowly varying). If I_{sc} is highly dynamic, then we expect the scheme to detect the fault perfectly, however, with possibly degraded fault estimation performance.

Next, we evaluate the robustness of the proposed scheme with respect several forms of uncertainties.

Robustness to Uncertain Basis Function: One of the enabling assumptions for our approach is *Assumption* 3. Here we illustrate the robustness of the scheme with respect to uncertain basis function $(\psi(\cdot,\cdot,\cdot))$. To inject uncertainty in the knowledge of basis function, the basis function for the plant (denoted by $\psi(\cdot,\cdot,\cdot)$) and the basis function used in the scheme (denoted by $\hat{\psi}(\cdot,\cdot,\cdot)$) are chosen to be different. To illustrate the findings, we choose the simulation scenario defined in *Case 2* with the same threshold value (0.02). In the first case, we choose the basis functions such that there is an overlap between $\psi(x)$ and $\hat{\psi}(x)$. The basis functions and corresponding fault diagnosis performance is shown in Fig.12. The fault estimation parameter $\hat{\theta}$ crosses the threshold $(th = 0.02)$ 0.7 sec after the fault occurrence at 300 sec,

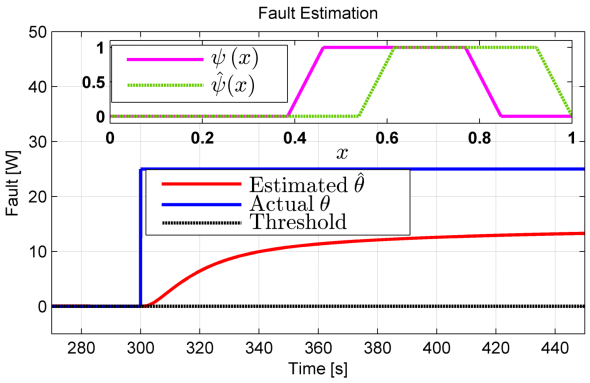

Fig. 12. Fault estimation performance under uncertain basis function $\psi(x)$. The functions $\psi(x)$ and $\hat{\psi}(x)$ denote the basis function used in plant and diagnostic scheme, respectively. There is some overlap between $\psi(x)$ and $\hat{\psi}(x)$. The simulation scenario is based on Case 2.

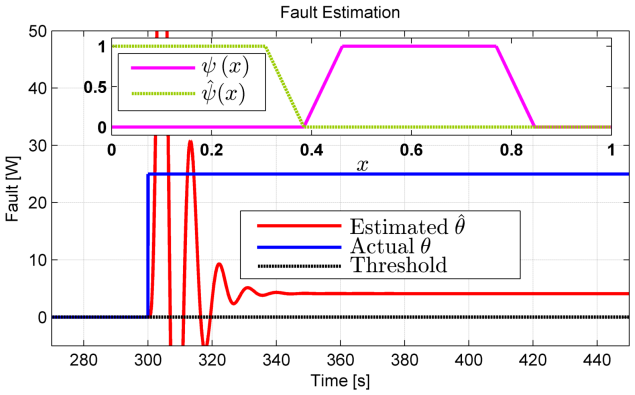

Fig. 13. Fault estimation performance under uncertain basis function $\psi(x)$. The functions $\psi(x)$ and $\hat{\psi}(x)$ denote the basis function used in plant and diagnostic scheme, respectively. In this case, there is no overlap between $\psi(x)$ and $\hat{\psi}(x)$. The simulation scenario is based on Case 2.

signaling a detected fault. However, the fault estimation error is approximately 50%. Next, we choose the basis functions such that there is no overlap between $\psi(x)$ and $\hat{\psi}(x)$. The basis functions and corresponding fault diagnosis performance is shown in Fig.13. The fault estimation parameter $\hat{\theta}$ crosses the threshold 0.8 sec after the fault occurrence at 300 sec, signaling a detected fault. However, the fault estimation error is much larger. From this study, we can conclude that the proposed scheme retains its detectability even when the basis functions are uncertain. However, the fault estimation performance degrades depending on the level of uncertainty.

Robustness to Parametric Uncertainties: In this study, we illustrate the robustness by examining the fault estimation errors under parametric uncertainties. The fault estimation error is defined as: $100(\theta - \hat{\theta}_{ss})/\theta$ where $\hat{\theta}_{ss}$ is the steady state value of the estimated fault $\hat{\theta}$. To inject parametric uncertainties, we deviate the crucial thermal parameters from their nominal values in the plant model while designing the observers based on the nominal parameter values. To illustrate the findings, we choose the simulation scenario defined in *Case 1* and treat the thermal parameters h, k and C_p as uncertain parameters. In the first case, we inject 10%, 25% and

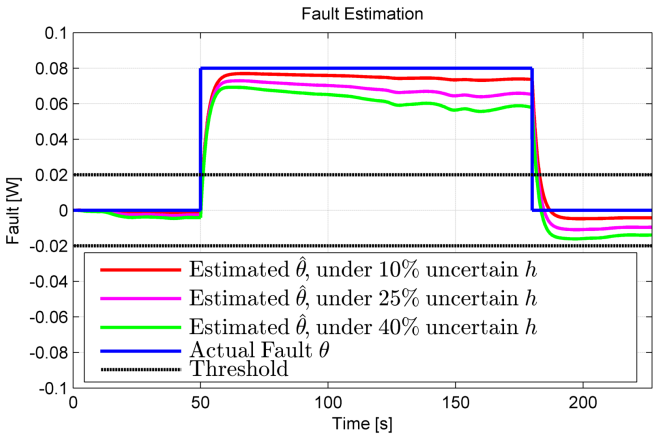

Fig. 14. Fault estimation performance under different levels of uncertainties in the parameter h. The simulation scenario is based on Case 1.

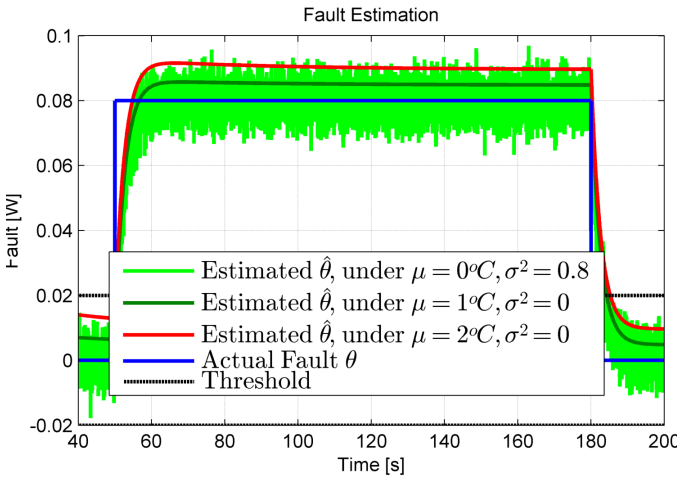

Fig. 15. Fault estimation performance under different levels of measurement noise $\mathcal{N}(\mu, \sigma^2)$. The simulation scenario is based on Case 1.

40% uncertainties in h which resulted in approximately 9%, 19% and 28% fault estimation error, respectively. The fault estimation performance is shown in Fig. 14. In the second case, we inject 10%, 25% and 50% uncertainties in k which resulted in approximately 1%, 5% and 9% fault estimation error, respectively. Finally, we inject 10%, 25% and 50% uncertainties in C_p which resulted in approximately 4%, 10% and 12% fault estimation error, respectively. From this study we can conclude that the proposed scheme is most sensitive to the parameter h, among the set $\{h, k, C_p\}$. Hence, parameter h should be known with sufficient accuracy to achieve an acceptable fault estimation error. To quantify the accuracy according to our study, the parameter h should be within 90% of its true value defining 10% fault estimation error as an acceptable limit. On the other hand, the scheme is comparatively more robust to the uncertainties in k and C_p and can handle approximately up to 50% inaccuracy in these parameters.

Robustness to Measurement Uncertainties: Next, we illustrate the robustness of the proposed scheme with respect to measurement uncertainties. To inject measurement uncertainties, we include additive noise in the surface temperature measurement with Gaussian distribution $\mathcal{N}(\mu, \sigma^2)$ where μ is mean and σ^2 is variance. Similar to the parametric uncertainties, we choose the simulation scenario defined in *Case 1* for illustration. In the first case, we inject measurement biases by specifying $\mu = 1^oC, \sigma^2 = 0$ and $\mu = 2^oC, \sigma^2 = 0$. The fault estimation error corresponding to these two biases are 5% and 10% respectively. In the second case, we inject measurement noise with $\mu = 0^oC, \sigma^2 = 0.8$. The fault estimation performance for these cases is shown in Fig. 15. From this study we have found that the proposed scheme is able to provide reasonable fault estimates when the measurement uncertainty has the following properties $\mu \leq 2^oC$ and $\sigma^2 \leq 1$. Here, reasonable fault estimate is defined by 10% or less error in fault estimation. Beyond these limits, the fault estimation performance is poor. The sensitivity of the scheme to high magnitudes of measurement uncertainties is due the high gain design of *Robust Observer*. In practice, the trade-off between fault suppression and measurement noise amplification should be considered while designing the *Robust Observer* parameter c in (24).

B. Experimental studies

In this section, we evaluate the effectiveness of the scheme using experimental data. The applied current profile for this experiment is same as shown in Fig. 4. The heat generation fault is injected by turning on the heating pad at the desired time to supply heat at $10W/in^2$ to the surface of the A123 battery cell. In this case we have $\psi(x, T(x,t), I(t)) = 1$ for $x = 1$, and $\psi(x, T(x,t), I(t)) = 0$ elsewhere. With this fault structure, the fault magnitude θ has been identified offline minimizing the difference between the model temperature and experimental temperature under faulty condition. Note that the identified θ is not provided to the online scheme and only used to validate the performance of the scheme.

The surface temperature under nominal and faulty cases are shown in Fig. 16, which clearly shows higher temperature under faulty condition. Similar to the simulation studies, we initialize the observers with incorrect temperatures except for the surface temperature as it is measured. Note that we only have experimental measurements/information of the surface temperature and injected fault. Therefore, we evaluate the effectiveness of the proposed scheme in terms of the surface temperature estimation error ($\tilde{T}_1(1)$ and $\tilde{T}_2(1)$) and fault estimation error ($\tilde{\theta}$). In Fig. 17, both $\hat{T}_1(1)$ and $\hat{T}_2(1)$ from the *Robust Observer* and *Diagnostic Observer*, respectively, tracks the true temperature $T(1)$ despite the mismatch between the experimental data and open-loop model evident in Fig. 16. Therefore, both the observers are able to track the true surface temperature even in the presence of fault and modeling uncertainties, as per the desired objective stated in Theorem 1 and Theorem 2. The steady-state estimation error for both the observers remain bounded within $0.2°$C. Furthermore, the fault estimation parameter $\hat{\theta}$ crosses the threshold shortly after the fault occurrence at 45 sec, thus detecting the fault. In this case, the detection time is 5 sec. Moreover, $\hat{\theta}$ converges to a neighborhood of the true fault

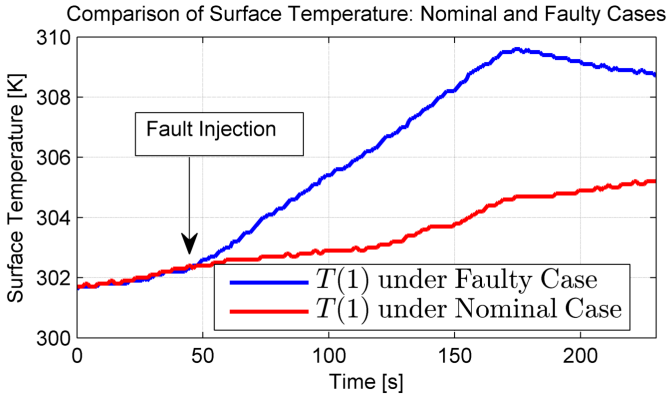

Fig. 16. Comparison of experimental surface temperatures under nominal and faulty conditions. For the faulty case, the fault was injected at 45 sec.

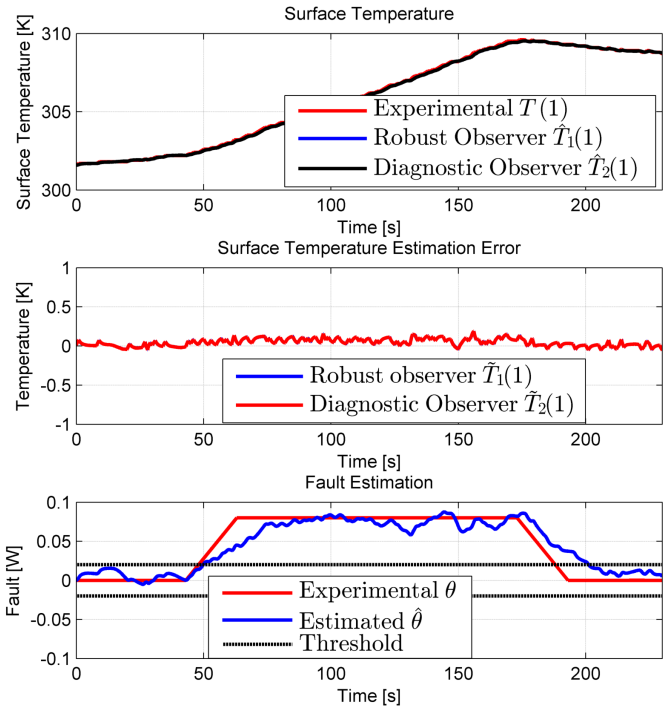

Fig. 17. Temperature and fault estimation performance. The fault is injected between 45 sec and 190 sec.

size θ with the steady-state error within $\pm 15\%$, as shown in the bottom subplot in Fig. 17. Note that the steady-state error of $\pm 15\%$ can be deemed reasonable considering the small magnitude of the injected fault and the presence of the modeling uncertainties. The estimate $\hat{\theta}$ converges to the $\pm 15\%$ band of the true fault size θ within 10 sec and remain within the band for subsequent times. Recall that Theorem 2 only guarantees boundedness of $\tilde{\theta}$, i.e. $|\tilde{\theta}| \in \mathbb{L}_\infty$. However, we find the estimate is a reasonable approximation of the actual fault size.

Remark 13. Fig. 16 shows that the surface temperature $(T(1))$ stays below 37^oC even after 2 minutes of consistent fault occurrence. Therefore, traditional limit checking approaches would consider this within normal operating temperature range resulting in a miss-detection of the fault. On the other hand, the proposed approach diagnoses the fault within 5 sec of its occurrence and estimates the fault size within 10 sec. This clearly shows the potential of the proposed approach in early diagnosis of the thermal faults.

V. Conclusion

This paper presents a PDE-observer based diagnostic scheme for diagnosing thermal faults in Li-ion batteries. We consider a distributed parameter thermal model coupled to a second order electrical model for diagnostic scheme design. The scheme consists of two PDE observers working in cascade. The first observer, *Robust Observer*, estimates the internal temperature distribution. We prove the distributed state estimate (i) converges exponentially to the true distributed temperature state under nominal conditions, and (ii) converges within a neighborhood of the true temperature state, which can be made arbitrarily small, under fault conditions. The second observer, *Diagnostic Observer*, utilizes this estimated temperature distribution and in turn detects and estimates thermal faults. We prove the fault estimation error $\tilde{\theta}$ is bounded in terms of the $\mathbb{L}_\infty$ norm. The proposed scheme is tested via simulation and experimental studies. Case 1 of the simulation study considers an internal heat generation fault. Case 2 considers an internal short circuit fault. Furthermore, the robustness of the scheme is evaluated under parametric uncertainties. The robustness study reveals relatively high sensitivity to the convective heat transfer coefficient h. Finally, the effectiveness of the scheme is tested using experimental faulty data from a commercial Lithium-ion cell under a additive heat generation fault. Simulation and experimental results illustrate the convergence and robustness properties of the proposed scheme.

References

[1] T. M. Bandhauer, S. Garimella, and T. F. Fuller, "A critical review of thermal issues in lithium-ion batteries," *Journal of The Electrochemical Society*, vol. 158, no. 3, pp. R1–R25, 2011.

[2] M. Charkhgard and M. Farrokhi, "State-of-charge estimation for lithium-ion batteries using neural networks and ekf," *Industrial Electronics, IEEE Transactions on*, vol. 57, pp. 4178–4187, Dec 2010.

[3] H. Rahimi-Eichi, F. Baronti, and M. Y. Chow, "Online adaptive parameter identification and state-of-charge coestimation for lithium-polymer battery cells," *IEEE Transactions on Industrial Electronics*, vol. 61, pp. 2053–2061, April 2014.

[4] A. E. Mejdoubi, A. Oukaour, H. Chaoui, H. Gualous, J. Sabor, and Y. Slamani, "State-of-charge and state-of-health lithium-ion batteries diagnosis according to surface temperature variation," *IEEE Transactions on Industrial Electronics*, vol. 63, pp. 2391–2402, April 2016.

[5] R. Klein, N. Chaturvedi, J. Christensen, J. Ahmed, R. Findeisen, and A. Kojic, "Electrochemical model based observer design for a lithium-ion battery," *Control Systems Technology, IEEE Transactions on*, vol. 21, pp. 289–301, March 2013.

[6] S. J. Moura, N. A. Chaturvedi, and M. Krstić, "Adaptive partial differential equation observer for battery state-of-charge/state-of-health estimation via an electrochemical model," *ASME Journal of Dynamic Systems, Measurement, and Control*, vol. 136, no. 1, p. 011015, 2014.

[7] S. Dey, B. Ayalew, and P. Pisu, "Nonlinear robust observers for state-of-charge estimation of lithium-ion cells based on a reduced electrochemical model," *Control Systems Technology, IEEE Transactions on*, vol. 23, pp. 1935–1942, Sept 2015.

[8] X. Lin, H. Perez, J. Siegel, A. Stefanopoulou, Y. Li, R. Anderson, Y. Ding, and M. Castanier, "Online parameterization of lumped thermal dynamics in cylindrical lithium ion batteries for core temperature estimation and health monitoring," *Control Systems Technology, IEEE Transactions on*, vol. 21, pp. 1745–1755, Sept 2013.

[9] M. Debert, G. Colin, G. Bloch, and Y. Chamaillard, "An observer looks at the cell temperature in automotive battery packs," *Control Engineering Practice*, vol. 21, no. 8, pp. 1035 – 1042, 2013.

[10] R. R. Richardson, P. T. Ireland, and D. A. Howey, "Battery internal temperature estimation by combined impedance and surface temperature measurement," *Journal of Power Sources*, vol. 265, pp. 254 – 261, 2014.

[11] C. Zhang, K. Li, J. Deng, and S. Song, "Improved real-time state-of-charge estimation of lifepo4 battery based on a novel thermoelectric model," *IEEE Transactions on Industrial Electronics*, vol. PP, no. 99, pp. 1–1, 2016.

[12] S. N. Motapon, A. Lupien-Bedard, L. A. Dessaint, H. Fortin-Blanchette, and K. Al-Haddad, "A generic electro-thermal li-ion battery model for rapid evaluation of cell temperature temporal evolution," *IEEE Transactions on Industrial Electronics*, vol. PP, no. 99, pp. 1–1, 2016.

[13] Y. Kim, S. Mohan, J. Siegel, A. Stefanopoulou, and Y. Ding, "The estimation of temperature distribution in cylindrical battery cells under unknown cooling conditions," *Control Systems Technology, IEEE Transactions on*, vol. 22, pp. 2277–2286, Nov 2014.

[14] J. Marcicki, S. Onori, and G. Rizzoni, "Nonlinear fault detection and isolation for a lithium-ion battery management system," in *ASME 2010 Dynamic Systems and Control Conference*, pp. 607–614, American Society of Mechanical Engineers, 2010.

[15] S. Dey, S. Mohon, P. Pisu, and B. Ayalew, "Sensor fault detection, isolation, and estimation in lithium-ion batteries," *IEEE Transactions on Control Systems Technology*, vol. 24, pp. 2141–2149, Nov 2016.

[16] S. Dey and B. Ayalew, "A diagnostic scheme for detection, isolation and estimation of electrochemical faults in lithium-ion cells," in *2014 ASME Dynamic Systems and Control Conference (DSCC)*, vol. 4 of *5*, 2014.

[17] A. Sidhu, A. Izadian, and S. Anwar, "Adaptive nonlinear model-based fault diagnosis of li-ion batteries," *IEEE Transactions on Industrial Electronics*, vol. 62, pp. 1002–1011, Feb 2015.

[18] S. Dey, Z. A. Biron, S. Tatipamula, N. Das, S. Mohon, B. Ayalew, and P. Pisu, "Model-based real-time thermal fault diagnosis of lithium-ion batteries," *Control Engineering Practice*, vol. 56, pp. 37 – 48, 2016.

[19] M. Balas, "Feedback control of flexible systems," *IEEE Transactions on Automatic Control*, vol. 23, no. 4, pp. 673–679, 1978.

[20] S. Dey, H. E. Perez, and S. J. Moura, "Thermal fault diagnostics in lithium-ion batteries based on a distributed parameter thermal model," in *American Control Conference (ACC), 2017*, pp. 68–73, IEEE, 2017.

[21] S. A. Hallaj, H. Maleki, J. Hong, and J. Selman, "Thermal modeling and design considerations of lithium-ion batteries," *Journal of Power Sources*, vol. 83, no. 12, pp. 1 – 8, 1999.

[22] M. Krstic and A. Smyshlyaev, *Boundary control of PDEs: A course on backstepping designs*, vol. 16. Siam, 2008.

[23] Y. A. Cengel and A. J. Ghajar, *Heat and Mass Transfer: Fundamentals and Applications, 5e*. McGraw-Hill, 2011.

[24] X. Lin, H. E. Perez, S. Mohan, J. B. Siegel, A. G. Stefanopoulou, Y. Ding, and M. P. Castanier, "A lumped-parameter electro-thermal model for cylindrical batteries," *Journal of Power Sources*, vol. 257, pp. 1 – 11, 2014.

[25] C. Forgez, D. V. Do, G. Friedrich, M. Morcrette, and C. Delacourt, "Thermal modeling of a cylindrical lifepo 4/graphite lithium-ion battery," *Journal of Power Sources*, vol. 195, no. 9, pp. 2961–2968, 2010.

[26] D. Doughty and E. P. Roth, "A general discussion of li ion battery safety," *Electrochemical Society Interface*, vol. 21, no. 2, pp. 37–44, 2012.

[27] S. Santhanagopalan, P. Ramadass, and J. Z. Zhang, "Analysis of internal short-circuit in a lithium ion cell," *Journal of Power Sources*, vol. 194, no. 1, pp. 550–557, 2009.